Field Observations of Swash Zone Currents Estimated with Near-Field Optical Remote Sensing

ALEXANDRA MUSCALUS,[a] STEVE ELGAR,[a] BRITT RAUBENHEIMER,[a] LEVI GORRELL,[a] AND CIARA DOOLEY[a]

[a] *Woods Hole Oceanographic Institution, Woods Hole, Massachusetts*

(Manuscript received 19 December 2024, in final form 8 April 2025, accepted 13 May 2025)

ABSTRACT: Currents in the swash zone on a sandy Atlantic coast beach estimated with near-field optical remote sensing by tracking breaking-wave-generated foam with particle image velocimetry (PIV) are similar to those measured with in situ acoustic Doppler velocimeters (ADVs). The observations were obtained from a 40-m-tall tower located about 60 m inland of the beach over a 2-month period, yielding 180 h of data during a wide range of incident wave and local foam conditions. A smaller, overlapping set of observations also was obtained from a drone. The remote sensing estimates of mean alongshore flows, and the magnitude and phase of cross-shore flows, are highly correlated with the in situ measurements. However, the remote sensing estimates tend to underestimate the in situ measurements of downrush flows and overestimate the uprush flows, with the differences becoming smaller as the amount of foam increases. Analysis with drone-based images suggests that higher image resolution improves agreement between remotely sensed and in situ measurements, particularly for time-averaged cross-shore flows, but a nadir view angle does not eliminate persistent cross-shore bias. The remote sensing estimates allow for swash zone currents to be estimated both across and along the swash zone with relatively high spatial resolution, and show strong cross-shore gradients, including direction reversals in alongshore currents. In addition, the remote sensing estimates indicate flow patterns associated with the formation of beach cusps during times of submergence when low-tide topographic surveys are not feasible.

KEYWORDS: Currents; Oceanic waves; In situ oceanic observations; Remote sensing; Surface observations

1. Introduction

The swash zone, where waves intermittently cover the beach, is important to nearshore sediment transport and geomorphology (Masselink and Russell 2006; Butt and Russell 2000; Elfrink and Baldock 2002; Masselink and Puleo 2006; Butt et al. 2007; Brocchini and Baldock 2008; Bakhtyar et al. 2009; Lanckriet et al. 2014; Chardón-Maldonado et al. 2016; Chen et al. 2023). Sediment transport is sensitive to the hydrodynamic processes within a swash cycle, which consists of an onshore-directed uprush as a wave runs up the beach (the "runup") and the subsequent offshore-directed downrush as that water recedes. Most swash zone research has focused on cross-shore processes and variability, but alongshore flow speeds can be similar to those in the cross-shore (Austin et al. 2011; Puleo et al. 2014, 2020) and are relevant to sediment transport (Jackson et al. 2017). Net sediment transport in the swash often is small compared with that within a single cycle, and therefore can be determined by a small number of high-impact events (Hughes et al. 1997; Blenkinsopp et al. 2011). Thus, understanding detailed swash hydrodynamics is important for predicting and modeling geomorphology change.

Swash hydrodynamics have been measured in the field with ducted impeller flowmeters (Hughes et al. 1997; Masselink and Hughes 1998; Puleo et al. 2000), electromagnetic current meters (Butt and Russell 1999; Austin et al. 2011; Puleo et al. 2020), acoustic Doppler velocimeters (ADVs) (Raubenheimer 2002; Guedes et al. 2013; Puleo et al. 2014; Brinkkemper et al. 2016; Puleo et al. 2020), and runup wires (Elgar and Guza 1985a; Raubenheimer et al. 1995; Raubenheimer and Guza 1996; Masselink and Hughes 1998). However, the thin, bubbly, and intermittent nature of swash flows poses challenges for sensor technology, and rapid sediment transport can bury or scour near-bed sample volumes. Remote sensing techniques avoid some of these challenges and can provide quality data at relatively high spatial resolution. For example, light detection and ranging (lidar) has been used to measure beach profiles and runup (Almeida et al. 2013; Henderson et al. 2022; O'Connor and Mieras 2022), swash surface profiles (Blenkinsopp et al. 2010; Ibaceta et al. 2018), and surfzone wave transformation (Brodie et al. 2015; Martins et al. 2017, 2020; Harry et al. 2018). Flow fields can be measured by tracking surface roughness in Doppler radar (Puleo et al. 2003; Perkovic et al. 2009) and regions of foam in time-averaged images (Chickadel et al. 2003; Power et al. 2011; Anderson et al. 2021). Swash fluctuations, runup heights, and the speed of the swash front can be obtained from series of instantaneous (nonaveraged) images (Stockdon et al. 2006; Senechal et al. 2011; Salatin et al. 2024).

Flow fields also can be estimated from the spatial lag of the maximum correlation of foam patches between successive images using particle image velocimetry (PIV) (Adrian 1984, 1991; Willert and Gharib 1991; Raffel et al. 2007). PIV often is used in laboratory investigations of swash (Cowen et al. 2003; Sou and Yeh 2011; Rivillas-Ospina et al. 2012) and has been adapted for field observations by georectifying undistorted images of the region of interest into real-world coordinates and using naturally occurring foam or heat as a tracer. PIV has been used to estimate mean currents in rivers (Puleo et al. 2012; Jessup et al. 2013; Tauro et al. 2017), tidal streams (McIlvenny et al. 2023), and the surfzone (Perkovic et al. 2009;

Corresponding author: Alexandra Muscalus, alexandra.muscalus@whoi.edu

DOI: 10.1175/JTECH-D-24-0156.1

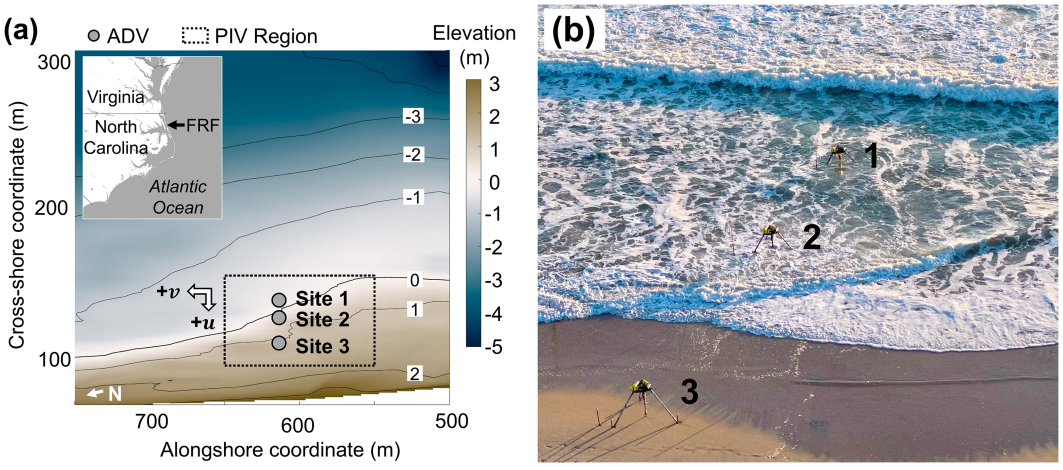

FIG. 1. (a) Contours of water depth (relative to NAVD88; scale on the right with curves every 1 m) as a function of cross- and alongshore coordinates. ADVs are shown with gray circles, and the camera FOV used here is indicated by the dashed-black rectangle. The FRF location in North Carolina is shown in the inset map on the upper left. (b) Photograph of the three ADV tripods, with a bore between sites 2 and 3 propagating ~30° relative to shore normal. Spatial coordinates are in the FRF coordinate system, which originates near the southern boundary of the FRF property and increases northward in the alongshore and seaward in the cross-shore directions.

Wilson et al. 2014; Elgar et al. 2023; Dooley et al. 2025), as well as wave orbital velocities in the swash and surfzones (Holland et al. 2001; Puleo et al. 2003; McCormack et al. 2025).

Here, cross- and alongshore velocities in the swash zone estimated with PIV using images from tower- and drone-mounted cameras (oblique and nadir viewpoints, respectively) are compared with velocities measured with in situ current meters for a wide range of conditions that include 180 h (spanning 2 months) of current estimates across the swash zone along 100 m of the shore. The remote sensing estimates of 2-Hz time series, power spectra, and 15-min flows are similar to those measured in situ at three locations across the swash zone.

2. Methods

a. Field site

Swash flows on a sandy Atlantic coast beach were observed from 27 August to 17 October 2021 at the U.S. Army Corps of Engineers Field Research Facility (FRF) in Duck, North Carolina (Fig. 1). Incident wave conditions were measured in 9-m water depth, and mean water levels were measured (NOAA station 8651370) at the end of the FRF pier. The tidal range is about 1 m, although water levels ranged from −0.8 to 1.4 m (all elevations are reported with respect to the NAVD88 datum) during the observations due to surge and setup. Significant wave heights H_s ranged from 0.2 to 2.9 m (Fig. 2), with the largest waves occurring during a nor'easter on 10 October.

b. In situ observations

In situ velocities were measured for 3072 s starting at the top of every hour at 8 Hz with ADV (Raubenheimer 2002) at three locations (sites 1–3) along a cross-shore transect spanning the swash zone at alongshore coordinate 615 m (Fig. 1). The ADVs were time synced using a Network Time Protocol server. As the beach eroded and accreted, the ADVs were adjusted vertically during low tides to maintain sample volumes less than 0.05 m above the bed. Consecutive data points with low correlations (below 0.53; Elgar et al. 2001, 2005), indicating poor-quality measurements owing to bubbles or other processes, were interpolated if spanning less than 1 s or (not including the first or last data point of the record) replaced with a 1-s running average if spanning more than 1 s. Segments of consecutive data points with low signal-to-noise ratios (SNRs), indicating the sensor not being submerged, and isolated points with high SNR bracketed by more than 1 s of low SNR values were replaced with not a number (NaN). Isolated low-SNR data points were replaced with interpolation, or if at the start or end of the record, with extrapolation. The resulting quality-controlled data were downsampled to 2 Hz for comparison with remote sensing estimates.

c. Tower images

Surface flows in the swash were estimated by tracking breaking-wave-generated foam in 2-Hz optical images from

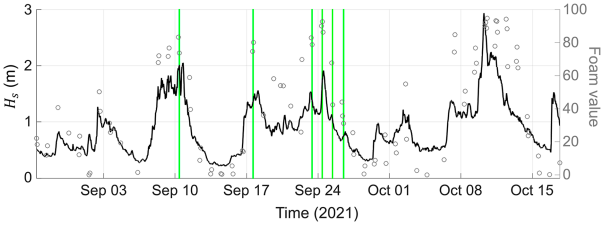

FIG. 2. Significant wave height in 9-m water depth (black curve, left axis) vs time. The gray circles indicate foam coverage (right axis), with a value of 100 corresponding to a swash zone fully saturated with foam. The vertical green lines indicate times of the example cases discussed below.

FIG. 3. Images from the tower in (a) low (foam value = 16%, H_s = 0.6 m), (b) medium (foam value = 38%, H_s = 1.1 m), and (c) high (foam value = 74%, H_s = 2.0 m) foam conditions. The black dotted rectangles bound the PIV region.

a 5.3-megapixel Genie Nano C2590 camera mounted on the top of a 40-m-tall tower (cross- and alongshore coordinates 34 and 584 m, respectively), and pitched 65° from horizontal. At the ADVs, raw pixel dimensions in the camera look direction (approximately cross-shore) and cross-look direction (approximately alongshore) were 0.17 m × 0.06 m at site 1 (most offshore), 0.14 m × 0.06 m at site 2 (central), and 0.10 m × 0.05 m at site 3 (most onshore). Images were recorded in five 2-h "runs" spanning daylight hours 0800 to 1800 local time (EDT). The images were time synced with a GPS clock.

Wind-induced tower vibration caused up-and-down camera motion corresponding to several pixels, so raw images were stabilized using control point registration to correct for several-pixel jitter. This technique translates a "moving" image into alignment with a fixed reference image using predefined image features, called "control points." Here, the control points are high-contrast edges of bright, stationary objects on the beach and pier.

Stabilized images were corrected for intrinsic lens distortion (Bouguet 2022), and pixel data were mapped to a 0.1-m-resolution spatial grid with georectification parameters computed from ground control points surveyed with GPS. Georectifying image data from pixel coordinates to a horizontal grid of spatial coordinates requires elevation data across the full field of view (FOV). Similar to surfzone studies, a constant elevation grid at the verified NOAA tidally varying mean water level is used seaward of the intersection with the beach, and to account for the effect of beach slope on thin swash flows rushing up and down the foreshore, surveyed beach elevations are used above the mean water level.

Beach elevation data were obtained primarily from hourly high-resolution lidar frame scans obtained with a RIEGL Z210i laser scanner at cross- and alongshore coordinates 51 and 620 m. For each camera run, beach elevations were compiled from the prior 24 h of lidar scans, prioritizing data from more recent scans. That is, the grid initially was populated with values from the most recent scan, and missing elevations iteratively were filled using older scans, provided data quality was sufficient. Thus, each location of the grid used the most recent high-quality elevation measurement available. Elevations seaward of the lidar range were obtained from vessel surveys conducted every few days.

d. *Drone video*

Swash imagery near the ADVs also was obtained from a 13-min, 24 fps video recorded with a pocket drone at a height of 29 m. Stabilization was performed using stationary equipment (e.g., sensor tripods) in the field of view that was a unique color and always at least partially unobscured. The equipment was isolated with color filtering, and the resulting images were aligned to an equivalently filtered reference image by maximizing full-image correlation through translation, rotation, and distortion. Georectification was performed using the surveyed locations of the sensors in the field of view.

e. *PIV*

Currents were estimated by tracking foam with PIV (Raffel et al. 1998; Adrian 1991; Perkovic et al. 2009; Dooley et al. 2025) using the open-source software PIVLab (Thielicke and Stamhuis 2014). The field of view is 60 m × 120 m in the cross- and alongshore directions (black dashed rectangles in Figs. 1 and 3). PIV was implemented using a multipass FFT algorithm applied to a 3.2 m × 3.2 m (32 × 32 pixels) initial interrogation window (Table 1), allowing for a maximum velocity of 6.4 m s^{-1} when using 2-Hz imagery. Two additional passes were applied, each halving the window dimension, with the final pass being 0.8 m × 0.8 m resolution (8 × 8 pixels) (Table 1). Lower image resolution (e.g., 0.15 m per pixel) produced lower-quality data, whereas higher 0.05 m per pixel resolution produced similar results at the expense of 4 times the

TABLE 1. PIV parameters used with the tower-mounted images.

PIVLab parameter	Value
Image frequency	2 Hz
Image resolution	0.10 m per pixel (cross-shore and alongshore)
Number of passes	3
Initial pass window size	3.2 m (32 pixels) × 3.2 m (32 pixels)
Second pass window size	1.6 m (16 pixels) × 1.6 m (16 pixels)
Third pass window size	0.8 m (8 pixels) × 0.8 m (8 pixels)
Window overlap	50%
Repeat last pass	On
Image deformation	Linear
Linear correlation	Off
Subpixel Finder	On

TABLE 2. Foam coverage, significant wave heights, and number of runs.

Foam coverage	Foam value range	Median H_s (m)	Number of 2-h runs
Low	0%–24%	0.5	36
Medium	25%–59%	0.9	24
High	60%–100%	1.5	31

computational time and data storage requirements. Similarly, increasing window sizes, decreasing window sizes, and reducing the number of window passes relative to those used (Table 1) produced noisier output. Velocities for which the cross correlation between sequential images was less than 0.2 were discarded. Increasing the correlation threshold significantly decreased data output without improving accuracy. Image preprocessing (such as contrast enhancement) increased computational time, but did not change output quality significantly, and thus was not implemented. PIV was run on the drone videos with the same algorithm, number of passes, and physical window sizes, with several image resolutions and frequencies compared with each other and with the tower-mounted images (discussed below).

PIV requires sufficient tracer particles in a window, so the foam conditions of each 2-h camera run were quantified with a subset of images. Nonwater regions in the FOV were identified by evaluating temporal pixel variance among an image subset, with low variance indicating unchanging regions. Pixels with temporal correlations greater than a reference value evaluated in a continuously dry region (a beach access road) were identified as dry beach and removed. The shoreline was defined as the onshore extent of the remaining high-variance (water coverage) region. The foam condition was assessed in a region that spanned alongshore coordinates 580–600 m, with its 100-m-wide cross-shore position varying with the shoreline position to account for variable mean water levels. In that region, brightness was evaluated using a composite image from each camera run, created by combining the maximum pixel intensities from three sample images. To minimize ambient lighting effects, the composite was treated with contrast stretching, mapping foam pixels to white and nonfoam pixels to black. The foam value was calculated as the percentage of pixels in the contrast-stretched composite with intensities of at least 98% of the maximum pixel intensity.

Foam values ranged from 0% to 100% and were correlated with H_s ($R^2 = 0.75$, Fig. 2). Each run was classified as either low, medium, or high foam (Table 2, Fig. 3), dividing the dataset into about thirds.

3. Results

To avoid contamination of the PIV estimates by the stationary tripods holding the ADVs, the PIV estimates are offset 5 m to the south in the alongshore. However, if waves are not normally incident, they arrive at the location of the PIV estimate at a different time than when they arrive at the ADV (Fig. 1b). For example, in 0.5-m depth, wave celerities are ~2.2 m s^{-1}, and thus a wave arriving at an angle relative to normal $\theta = 10$ (30)° would require ~0.4 (1.1) s to travel 5 m south in the alongshore [i.e., $5 \times \sin(\theta)/2.2$]. Alongshore differences in the bathymetry (e.g., different beach slopes) also can result in small phase lags between velocities observed at the spatially separated locations. To align the ADV and PIV time series despite the temporally changing phase lags, the two time series were synchronized using dynamic time warping (DTW; Wang and Gasser 1997; Senin 2008). This technique nonlinearly warps the time axis of one series to optimize phase synchronization with a second series. The sequence of data points is maintained, but time is stretched and compressed to minimize

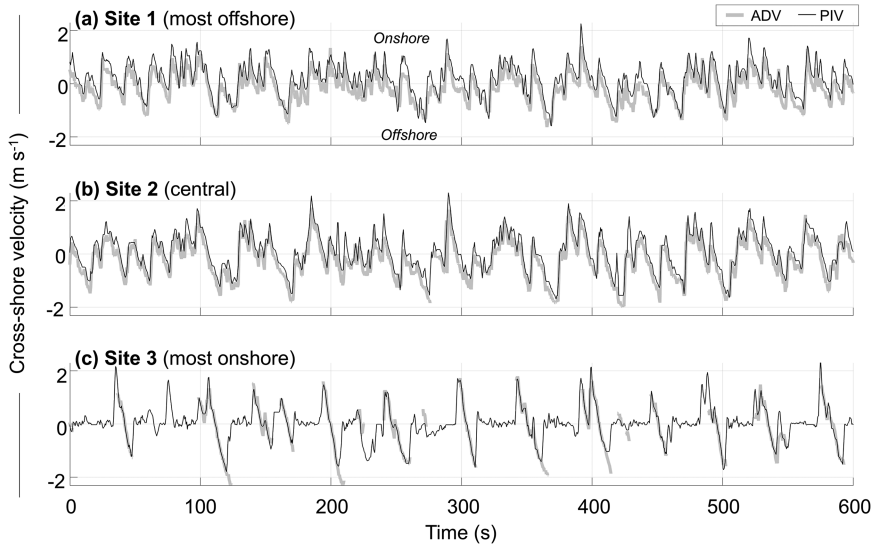

FIG. 4. Cross-shore velocity (2 Hz) vs time at sites (a) 1, (b) 2, and (c) 3 at about 1100 EDT 10 Sep 2021 estimated with PIV (black curves) and ADVs (thick gray curves).

the cumulative distance (discrepancies) between corresponding data points, synchronizing dominant signals. Here, DTW was applied to the PIV time series and constrained to a maximum time shift of 3 s. Synchronization results in improved correlations between PIV estimates and ADV measurements of time series for both cross- and alongshore velocities. If a data point was missing from one time series, it was removed in the other time series. Missing data points were treated as NaN for all analyses except computing spectra, where NaNs were temporarily replaced with zeros.

Time series (Fig. 4) of cross-shore flows u for a high-foam case (10 September 2021, Fig. 3c) estimated with PIV are similar to those observed with the in situ ADVs. The PIV-estimated onshore flows are stronger, whereas the offshore flows are weaker than those measured by the ADVs, and thus the PIV u are shifted onshore of the ADV u (Fig. 4). When located near the onshore edge of the swash zone, ADVs (~0.05 m above the bed) are intermittently submerged (Fig. 4c), and measure only the deepest flows, including the transition from peak uprush (most positive u) to peak downrush (most negative u). In contrast, PIV estimates the flows nearly continuously, although sometimes maximum downrush flows are significantly less than those observed with the ADVs (Fig. 4c).

Both cross-shore u and alongshore v spectra from PIV (DTW-synchronized data) and ADV estimates are similar to each other for the high-foam case of 10 September (Fig. 5), especially at the energetic infragravity ($f = 0.02$ Hz, where f is frequency) and swell ($f = 0.06$ Hz) peaks in cross-shore spectra. In contrast to the cross-shore velocities, neither alongshore velocity estimation technique includes a significant infragravity peak. At both sites, the PIV v spectral levels are more energetic than the ADV v spectral levels (cf. dotted black with dotted-gray curves in Fig. 5). Magnitudes of PIV-based u and v spectra are larger than those for the ADV at both locations, and thus differences cannot be owing to a coordinate system rotation and leakage of velocities between directions.

For the 180 h of data obtained over 2 months with a wide range of incident wave conditions (Fig. 2), time series (2 Hz) of velocities estimated with PIV are correlated with those observed with a neighboring ADV (Fig. 6), with increasing correlation as the amount of foam increases (from left to right across each row in Fig. 6). PIV estimates typically are biased onshore (positively) relative to the ADV measurements. Although most data fall near the 1:1 line, the scatter and root-mean-square differences (RMSD) indicate that the PIV sometimes underestimates strong onshore and offshore ADV flows (Figs. 6a,d–f). Differences are larger closer to shore and may result from insufficient foam for tracking, flow spatial variability, or phase differences not fully corrected by DTW. Binned (0.2 m s^{-1} bin widths) velocities (not shown) have higher correlations ($R^2 > 0.9$ for each case in Fig. 6).

To compare mean currents, ADV and PIV flows were averaged in 15-min, nonoverlapping segments with at least 50% data coverage. Combining measurements from the three sites results in 927 15-min mean flow estimates, with 34%, 27%, and 39% from low-, medium-, and high-foam conditions,

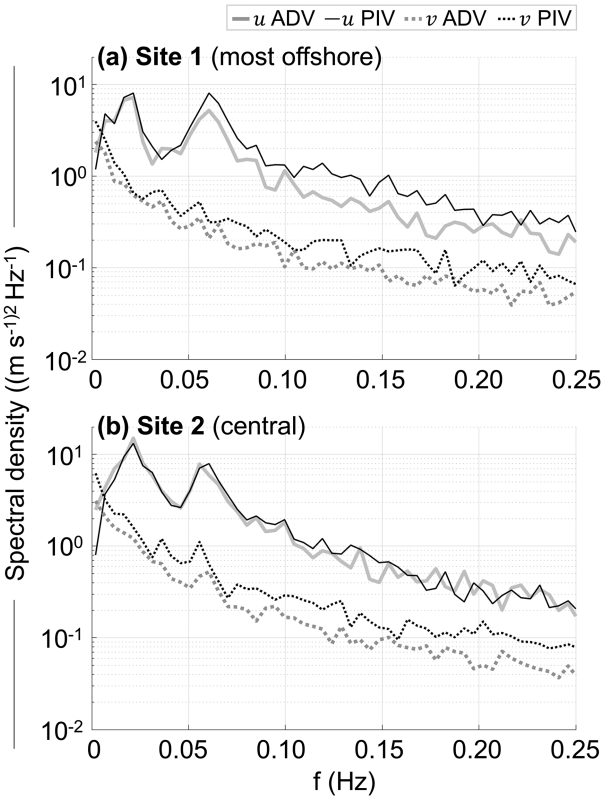

FIG. 5. Spectral density vs frequency for cross-shore (u, solid curves) and alongshore (v, dotted curves) from (a) site 1 and (b) site 2 computed from 2-Hz PIV (black) and ADV (gray) data from 1000 to 1159 EDT 10 Sep 2021 (10 min of the time series are shown in Fig. 4). The spectra were processed with 50% overlap of seven 2048-point (1024 s) segments with five neighboring frequency bands merged, resulting in 70 degrees of freedom and a frequency resolution of 0.005 Hz.

respectively. Mean cross-shore flows $\overline{u}$ estimated with PIV are weakly correlated with the means measured with the ADVs (Table 3) and are biased onshore relative to the means measured by the ADVs (cf. points with the 1:1 line in Fig. 7a), regardless of foam (symbol colors in Fig. 7) or wave conditions (not shown). Furthermore, in low-foam conditions, PIV can produce unusually large (>1 m s^{-1}) $\overline{u}$ values (blue symbols in Fig. 7a). The PIV may estimate large $\overline{u}$ in low foam because the onshore-moving bore has sufficient foam to be tracked by PIV and dominates the signal, whereas the limited foam remaining in the downrush can be insufficient to track. When there are few or no moving tracers in the PIV window, the spatial offset of maximum image correlation is about zero. Thus, the PIV estimates report near-zero downrush velocities in low foam, resulting in an onshore-directed bias.

Although alongshore orbital velocities are an order of magnitude smaller than cross-shore orbital velocities (Fig. 5), the magnitudes of mean cross- and alongshore currents are similar. PIV and ADV estimates of cross-shore currents are only weakly correlated with each other (Fig. 7a and Table 3) and do not exhibit a relationship with tidal stage (not shown), but

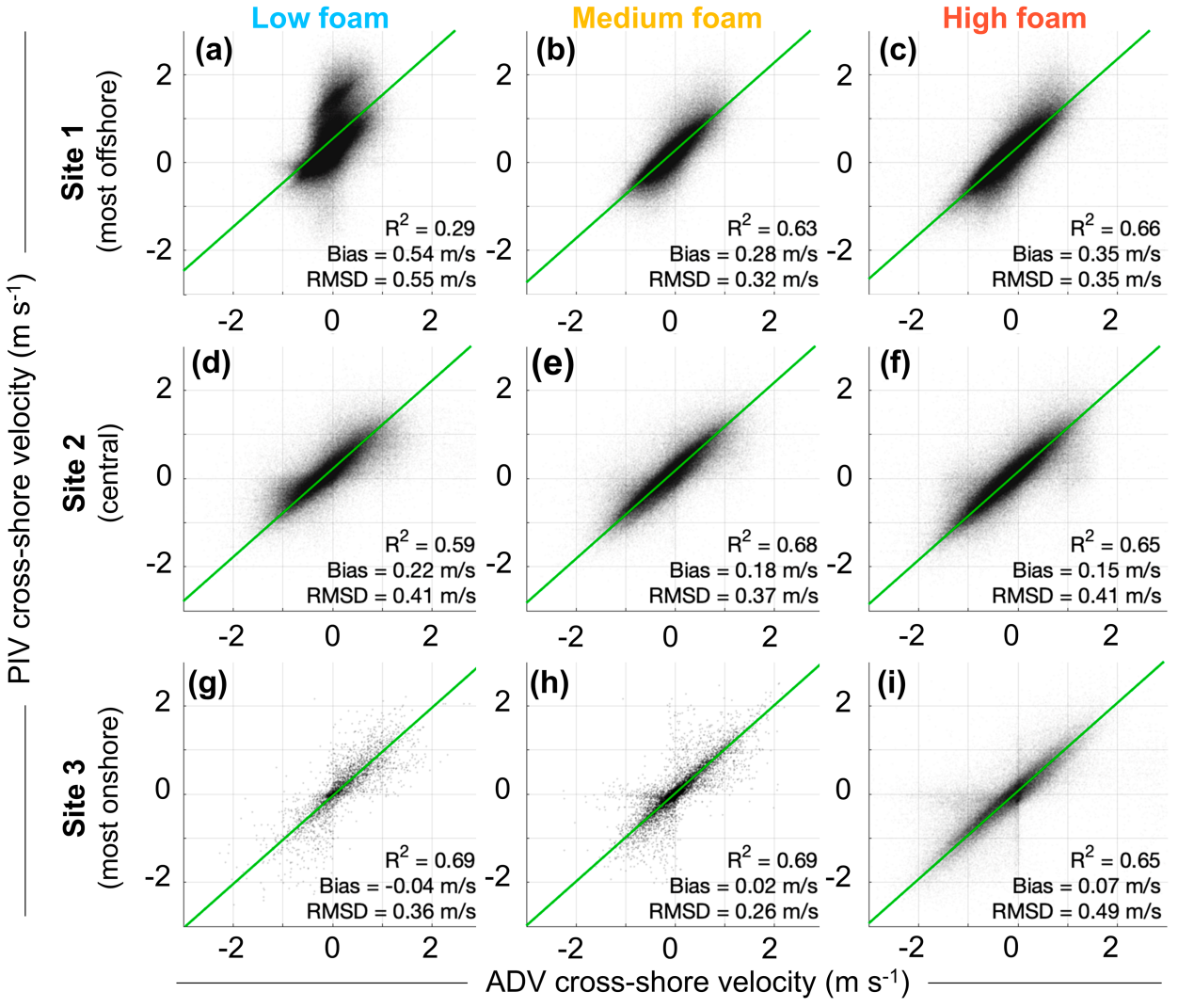

FIG. 6. The 2-Hz cross-shore velocities estimated with PIV vs 2-Hz cross-shore velocities measured by the ADVs for (left) low-, (center) medium-, and (right) high-foam conditions at sites (a)–(c) 1, (d)–(f) 2, and (g)–(i) 3. Correlations (R^2), bias (a positive value indicates an onshore bias), and demeaned RMSD are listed on each panel, and 1:1 relationships offset by the bias are shown by the green lines. The darkness of the point clouds increases with the number of points at each value.

PIV and ADV measurements of alongshore flows are correlated with each other (Fig. 7b and Table 3). The alongshore flow correlation increases with foam level (Table 3) from $R^2 = 0.7$ to $R^2 = 0.9$, and overall correlation and root-mean-square differences are similar to those reported for time-averaged alongshore surfzone flows (R^2 of 0.8, RMSD of 0.2 m s^{-1}) measured with remote sensing at this site (Dooley et al. 2025). However, the PIV tends to produce greater $\overline{v}$

TABLE 3. Correlations (R^2) of PIV with ADV statistics for different foam levels.

Characteristic	R^2		
	Low foam	Medium foam	High foam
Significant cross-shore velocity, u_s	0.10	0.76	0.79
Significant alongshore velocity, v_s	0.03	0.60	0.71
Cross-shore velocity centroidal frequency, $f_{c,u}$	0.68	0.98	0.98
Alongshore velocity centroidal frequency, $f_{c,v}$	0.15	0.72	0.72
15-min averaged cross-shore velocity, $\overline{u}$	0.32	0.25	0.33
15-min averaged alongshore velocity, $\overline{v}$	0.66	0.85	0.92

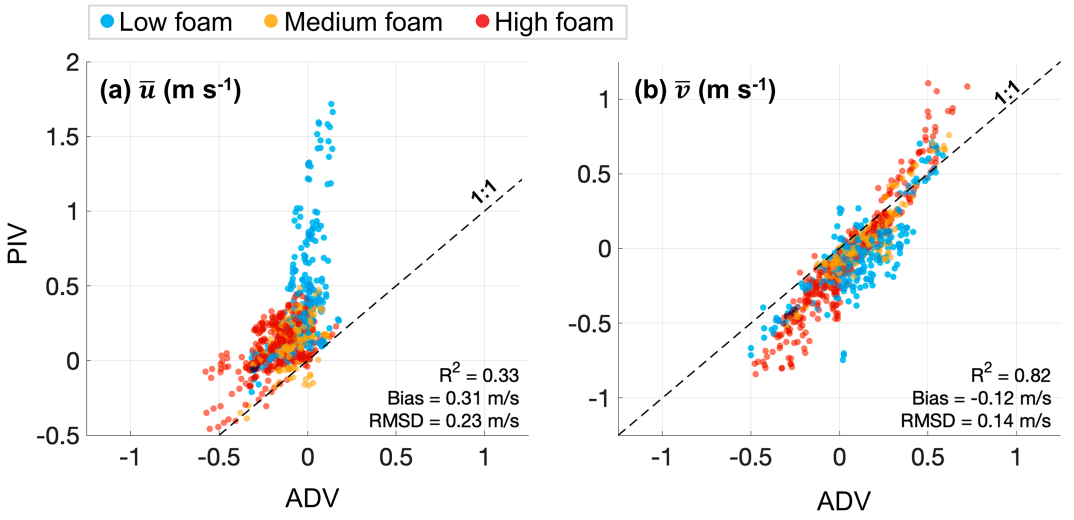

FIG. 7. The 15-min mean (a) cross- and (b) alongshore currents estimated with PIV vs mean currents measured with the ADVs. Symbol color indicates foam level (legend on the upper left). Correlations (R^2), bias (a positive value indicates an onshore bias for cross-shore flows and a northward bias for alongshore flows), and demeaned RMSD computed from data of all foam levels are listed on each panel.

magnitudes than the ADV in both alongshore directions (Fig. 7b), with the differences increasing as the amount of foam increases (see vertical variability of point colors at ADV $\overline{v} = -0.5$ and 0.5 m s^{-1} in Fig. 7b). This discrepancy could be caused by wind stress inducing stronger flows at the surface (the PIV measurement) and bottom friction causing weaker flows lower in the water column (the ADV measurement).

The correlations of PIV with ADV mean flows and significant currents [$4\sqrt{\mathrm{var}(u)}$ and $4\sqrt{\mathrm{var}(v)}$, evaluated for $0.05 < f < 0.25$ Hz, an estimate of the energy of the time series] typically increase with foam (colors in Figs. 8a,b, Table 3).

In the cross-shore, the correlations between PIV and ADV estimates of centroidal frequencies of the power spectra for $0.05 < f < 0.25$ Hz are high (Fig. 8c, Table 3) and increase as the foam values increase. In the alongshore, correlations of PIV and ADV centroidal frequency ($f_{c,v}$) are somewhat lower (Fig. 8d, Table 3), where spectral levels are an order of magnitude lower and spectral shapes are flatter (Fig. 4).

The effects of viewing angle, image spatial resolution, and frequency can be assessed by comparing oblique tower-mounted camera views with the nadir views from a drone (Dooley et al. 2025). The raw drone footage, recorded from a nadir viewpoint, has finer spatial resolution and a higher frame rate (24 Hz) than the tower camera. Prior to PIV analysis, the drone image data were interpolated to a uniform grid of either 0.05 or 0.10 m per pixel spatial resolution sampled at either 2 or 4 Hz. After computing skewness and asymmetry from the unaltered PIV time series, all instantaneous PIV flows were synchronized to the ADV signal with DTW. Flow time averages were computed with moving means after interpolation to a common 2-Hz time stamp and removal of bad data points. Comparisons are made at site 1, the most offshore position, because it has the greatest ADV data coverage.

All drone PIV cross-shore flow time series are well correlated with the ADV and tower PIV time series, and all tower and drone PIV cross-shore flows are biased similarly relative to the ADV measurements (Table 4, Figs. 9a–c). The onshore bias of remotely sensed cross-shore flows is about 0.4 m s^{-1} for the tower PIV, and all drone PIV variations considered, suggesting it is not attributed to image resolution, sampling frequency, or viewing angle.

The variations in spatial and temporal resolution in the drone PIV imagery produced statistically different cross-shore currents at site 1 at the 5% significance level (chi-square and Kolmogorov–Smirnov tests), although the statistics of the drone-estimated currents using different resolutions are similar to each other (Table 4). Time series skewness and asymmetry varied slightly among the measurement methods from 0.13 to 0.41 and 0.55 to 0.98, respectively, but with large uncertainty ranges (about ±0.4) due to the limited duration of the dataset. The skewness and asymmetry indicate peaked wave crests and forward-pitched sawtooth waves, typical of inner surf and swash zone conditions (Elgar and Guza 1985b; Raubenheimer and Guza 1995).

The drone cross-shore PIV flows processed with finer spatial resolution (0.05 m, Fig. 9b) agreed best with the ADV, with the strongest correlation and lowest RMSD (Table 4). Compared with the drone PIV processed with 0.10-m-resolution imagery, the 0.05-m-resolution PIV measured weaker uprush velocities more consistent with the ADV measurements (cf. drone-estimated peak uprush velocities with each other and with ADV measurements from 80 to 100 s in Figs. 9a,b), resulting in lower skewness (Table 4) than the other PIV applications. The drone cross-shore PIV flows processed at finer temporal resolution (4 Hz, Fig. 9c) are not statistically different than lower-frequency PIV estimates with the same spatial resolution (Table 4). The drone cross-shore PIV flows processed at finer

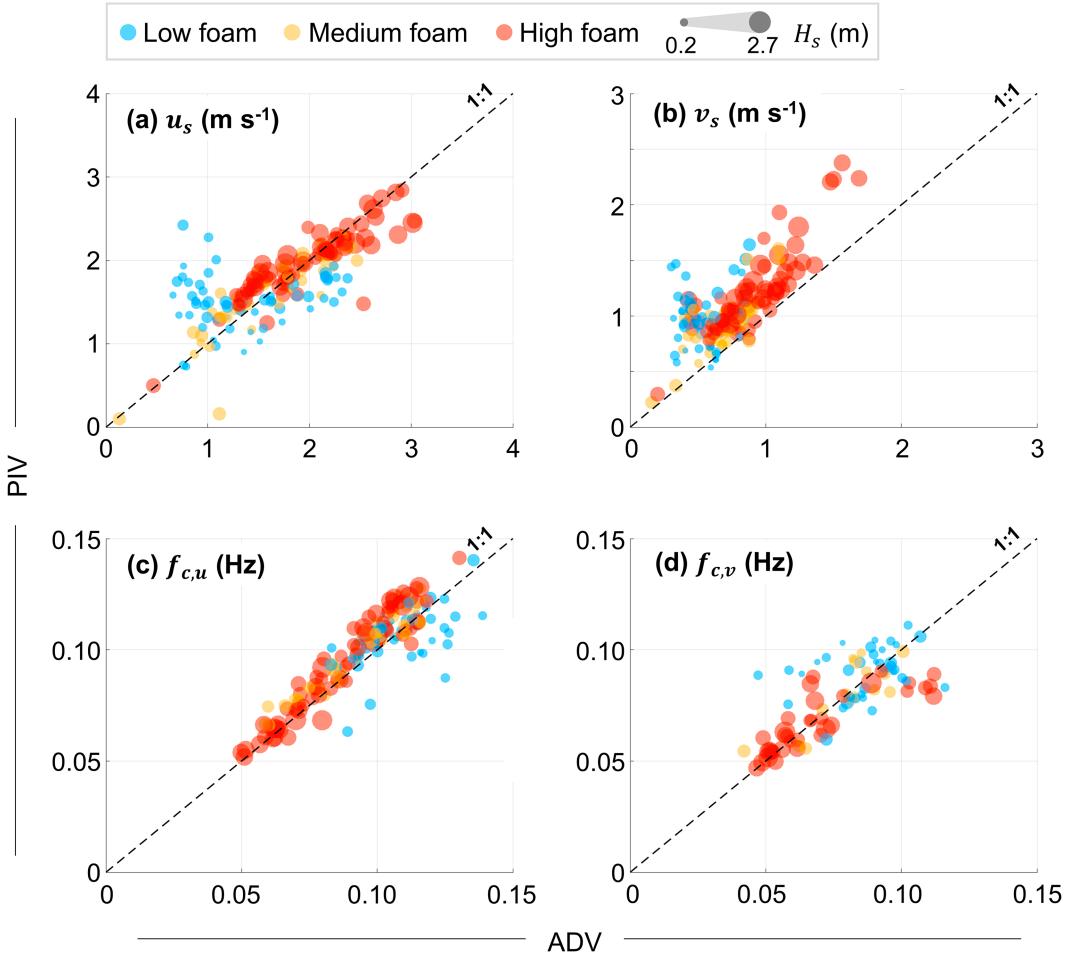

FIG. 8. PIV significant velocity in the (a) cross-shore (u_s) and (b) alongshore (v_s) directions and PIV centroidal frequency (f_c) of the (c) cross- and (d) alongshore flow spectra vs those statistics estimated with the ADVs for all cases with at least 75% PIV and ADV data coverage. Symbol color indicates foam level (legend on the upper left), and symbol size indicates incident significant wave height H_s. Axis limits differ in (a) and (b).

temporal resolution (4 Hz, Fig. 9c) differed slightly from the lower-frequency estimates, but the differences were smaller than those associated with the increased spatial resolution.

The estimates of mean alongshore currents (Fig. 9d) are similar for all the drone processing parameters (cf. the colored curves in Fig. 9d with each other). The time-averaged drone and tower PIV alongshore flows at site 1 (Fig. 9d) and site 2 (not shown) shift southward (negatively) of the ADV flows, resulting in differences of about 0.1 m s^{-1}. Due to the stability of the tower-mounted camera and stabilization applied to drone footage, this shift is unlikely to be caused by camera motion and may instead reflect spatial alongshore flow variability (all remote sensing measurements are offset 5 m in the alongshore from the ADV measurements).

TABLE 4. Comparisons of PIV with ADV cross-shore flow measurements and time series properties [skewness and asymmetry ("asymm")] at site 1 (most offshore position).

	Comparisons with ADV measurements			Time series property[a]	
Measurement	R^2	RMSD (m s^{-1})	Bias (m s^{-1})	Skewness	Asymm
0.10-m, 2-Hz tower PIV	0.65	0.35	0.38	0.32	0.60
0.10-m, 2-Hz drone PIV	0.71	0.29	0.39	0.33	0.76
0.05-m, 2-Hz drone PIV	0.77	0.24	0.39	0.13	0.55
0.10-m, 4-Hz drone PIV	0.73	0.30	0.38	0.41	0.98

[a]Uncertainty at the 95% confidence level is about ±0.4 for skewness and asymmetry.

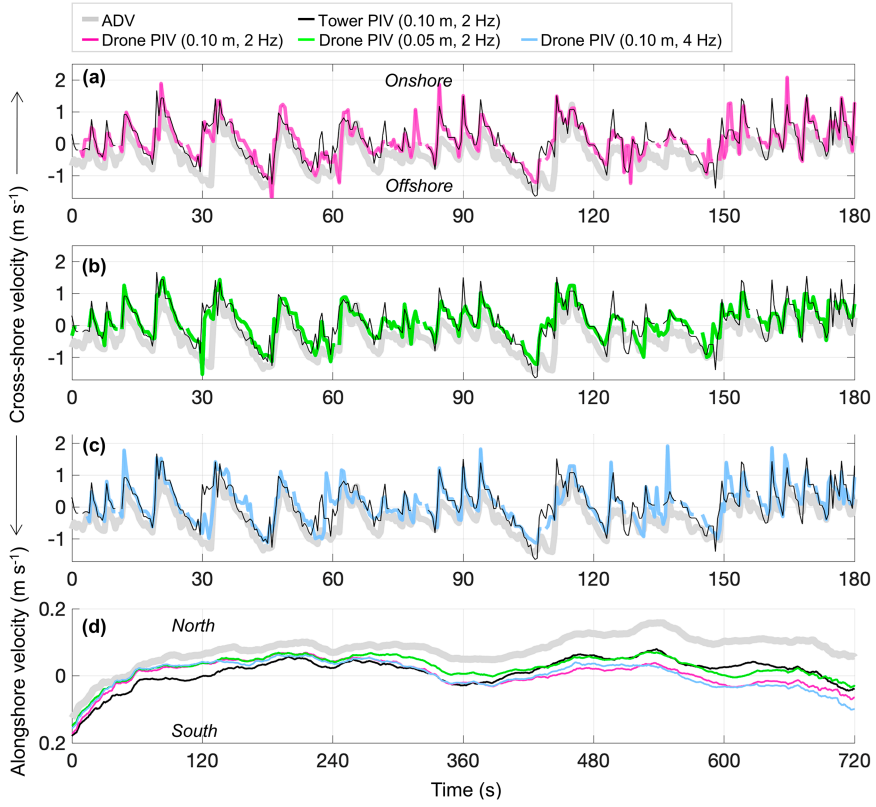

FIG. 9. (a)–(c) The 2–4-Hz cross-shore currents and (d) 5-min running means of alongshore currents at site 1 measured at about 1530 EDT 17 Sep 2021 with an ADV (gray curves), tower PIV (black curves), drone PV at 2-Hz and 0.10-m resolution [pink curves in (a) and (d)], drone PIV at 2-Hz and 0.05-m resolution [green curves in (b) and (d)], and drone PIV at 4-Hz and 0.10-m resolution [blue curves in (c) and (d)] vs time. Positive flows are onshore in (a)–(c) or to the north in (d).

The comparisons of drone and tower PIV estimates suggest that higher spatial resolution may reduce the discrepancy between ADV and PIV cross-shore flows (Table 4) more effectively than increased temporal resolution. However, after georectification, the raw tower images have coarser spatial resolution, with pixel dimensions ranging from 0.06 to 0.17 m, than the raw drone video, which has about 0.02-m pixel dimensions. Thus, interpolating tower images to 0.05-m resolution provides only a modest improvement in the agreement of tower PIV with ADV measurements (R^2 of 0.67 and RMSD of 0.28 m s^{-1}) compared with the improvement observed for the drone video, but quadruples data storage and processing needs.

4. Discussion

Although swash flows estimated with the tower-mounted camera are similar to those measured by the ADV, there are differences between the time series. Relative to the ADV, the PIV tends to measure stronger uprush flows, weaker downrush flows, and more zero or near-zero flows. These effects contribute to differences in mean cross-shore flows, particularly in low-foam (small wave) conditions (Fig. 7a).

Image factors contributing to the differences may include resolution limitations and the oblique viewing angle of the camera, which causes raw pixel size to increase (resolution to decrease) with distance from the camera, as well as disparities in look direction and cross-look direction raw pixel lengths. In real-world coordinates, pixel resolution is finer in the cross-look direction by about a factor of 2. Physical factors may include unequal amounts of foam on the uprush and downrush, flow differences between the PIV and ADV locations, and vertical flow variability.

Georectifying with a nonwave-resolving elevation grid induces false motion owing to the time varying water surface and is particularly sensitive to rapid changes in water slope. The time average of this false motion is zero if all phases of the wave are measured consistently, but a net effect is possible if the PIV misses a particular phase of the swash cycle, most commonly the downrush (Holland et al. 2001). Therefore, the false velocities were evaluated directly using wave-resolving lidar observations of the water surface along a transect at alongshore coordinate $y = 620$ m, near the location of the ADVs. For each ADV location, an elevation time series was obtained from the nearest point of the lidar transect. The pixel at that location was georectified into real-world horizontal coordinates

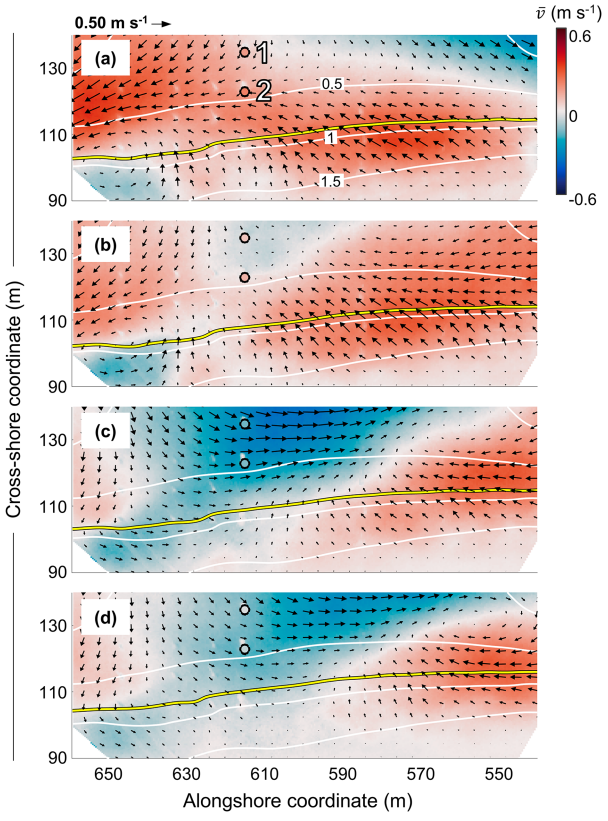

FIG. 10. Color contours of 15-min mean alongshore flows estimated with the tower PIV (scale on upper right) as a function of cross- and alongshore coordinates, with mean current vectors (every 10th is shown; scale at upper left) and contours of bathymetry [white curves, labeled in (a), and yellow curves are mean water level] at (a) 1000, (b) 1030, (c) 1100, and (d) 1130 EDT 10 Sep 2021. ADV measurements of 15-min mean alongshore flow (circles with color shading giving the strength of the alongshore flow) are shown at sites 1 and 2 [labeled in (a)].

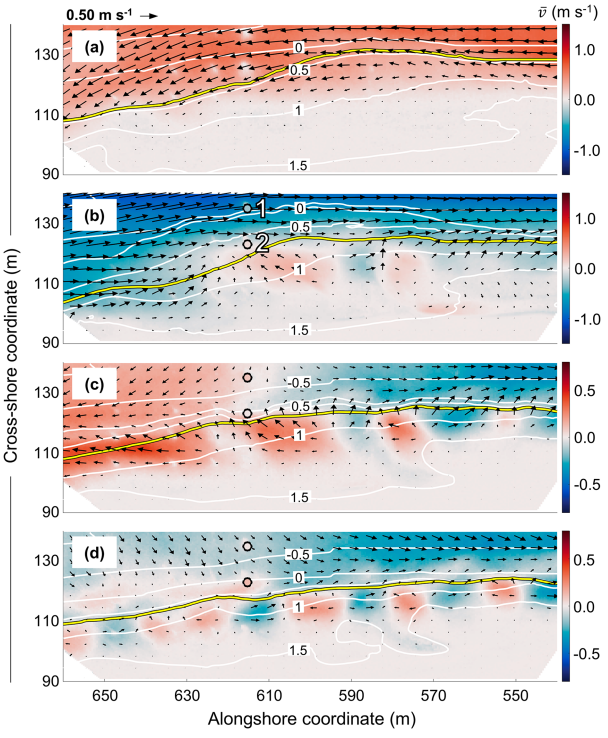

FIG. 11. Color contours of 15-min mean alongshore flows estimated with the tower PIV (scales on upper right) as a function of cross- and alongshore coordinates, with mean current vectors (every 10th is shown; scale at upper left) and contours of bathymetry (white labeled curves, with yellow curves at mean water level) around the daytime high tide on (a) 23 Sep, (b) 24 Sep, (c) 25 Sep, and (d) 26 Sep. ADV measurements (when available) of alongshore flow (circles with color shading giving the strength of the alongshore flow) are shown at sites 1 and 2 [labeled in (b)].

using the water surface elevation time series, creating a time series of horizontal position. The time derivative of that time series is the apparent velocity induced by elevation variations, or the "false velocity." However, removing this false velocity from the PIV results did not improve the agreement between the remote and in situ measurements.

With the available data, it cannot be determined if and when the ADV or PIV is more accurate. The two techniques operate on different principles, measure different quantities, and are subject to different sources of error. The ADV measures the velocity of suspended particles at depths sufficient to cover the sensor. When near the bed, the ADV may be in the boundary layer, and when above the bed may not be submerged when a low-elevation swash passes it. The PIV measures the motion of foam on the water surface, which can be influenced by wind stress and may or may not represent swash velocities beneath the surface. Thus, perfect agreement between the ADV and PIV is not expected.

Unlike the spatially sparse in situ sensors, PIV can estimate flows at high spatial resolution over large areas. For example, on 10 September, time-averaged alongshore flows at the ADVs changed direction several times surrounding high tide (circles at the ADVs in Fig. 10). The 15-min-averaged PIV flow fields spanning a 2-h period show large-circulation features that move and evolve (Fig. 10). For instance, at 1000 EDT (Fig. 10a), most of the region is dominated by northward (positive, red contours) flow, but a region of southward (negative, blue contours) alongshore flow appears near cross- and alongshore coordinates 130 and 610 m by 1030 EDT (Fig. 10b). The southward flow increases in strength and area and splits the region of northward flow (Fig. 10c), ultimately causing southward flow to dominate along the shoreline (Fig. 10d).

The large spatial area covered by the tower-mounted camera also allowed observation of evolving beach cusp circulation cells during cusp submergence (Fig. 11). Over 4 days, the flow field evolved from mostly alongshore uniform to the north (red contours in Fig. 11a) to mostly alongshore uniform to the south below 0.5-m elevation with the beginning of circular flow patterns near the 1.0-m depth contour (Fig. 11b). The flows became more alongshore inhomogeneous by the third day (Fig. 11c), with opposing alongshore currents below

0-m elevation and stronger circulation cells above 0-m elevation (Fig. 11c). By day 4, the flow was to the south below 0.5-m elevation, with distinct cusp-like circulation cells higher on the beach (Fig. 11d). The cusps were observed nearly continuously over several days during intermittent to constant submergence, permitting analysis of their evolution at higher frequencies than feasible with traditional topographic surveys and complementing lidar techniques (O'Dea and Brodie 2024) that measure dry beach bed levels.

5. Conclusions

Cross- and alongshore velocities estimated by tracking foam in 2-Hz sequential images of the swash zone with particle image velocimetry (PIV) are similar to velocities measured with in situ acoustic Doppler velocimeters (ADVs) within the field of view of a tower-mounted camera for a wide range of conditions.

Relative to ADV observations, the PIV foam tracking estimates weaker offshore flows and stronger onshore flows. The agreement between ADV and PIV currents varies with cross-shore location, and increases as the amount of foam increases, which is correlated with incident wave significant wave height. PIV estimated spectra are similar to those estimated with the ADVs, with correlations of significant velocities and centroidal frequencies increasing with increasing foam levels. Fifteen-minute mean alongshore currents estimated with PIV are strongly correlated with ADV measurements, whereas mean cross-shore currents estimated with PIV are weakly correlated with ADV measurements. PIV estimates of mean cross-shore currents, especially during low-foam conditions, are onshore of ADV measurements, possibly owing to insufficient foam during downrush.

Comparing PIV estimates from images obtained with a drone with those from the tower-mounted camera using the same processing details suggests correlations with the in situ ADVs are increased when the drone images are processed with higher frequency and spatial resolution. The nadir view angle of the drone does not reduce cross-shore flow bias.

The results suggest that provided sufficient foam, PIV performed on rapid sequences of images obtained with cameras mounted on a tower or a drone can produce high spatial resolution (0.1 m) flow fields across and along the swash zone of an ocean beach.

Acknowledgments. We thank the FRF field team, and Jinshi Chen, Drude Christensen, Matthew Florence, Enrique Padilla, and Laura Szczyrba for deploying and maintaining in situ and remote sensors in often difficult conditions, and Jinshi Chen for providing drone video. Funding was provided by the USCRP, NSF, and the WHOI Build the Base program. The authors have no conflicts of interest to declare.

Data availability statement. The full ADV dataset is available online at https://doi.org/10.5281/zenodo.14457084 (Raubenheimer et al. 2024). Image and lidar data (about 15 TB combined) can be accessed via discussion with the authors.

REFERENCES

Adrian, R. J., 1984: Scattering particle characteristics and their effect on pulsed laser measurements of fluid flow: Speckle velocimetry vs particle image velocimetry. *Appl. Opt.*, **23**, 1690–1691, https://doi.org/10.1364/AO.23.001690.

——, 1991: Particle-imaging techniques for experimental fluid mechanics. *Annu. Rev. Fluid Mech.*, **23**, 261–304, https://doi.org/10.1146/annurev.fluid.23.1.261.

Almeida, L. P., G. Masselink, P. Russell, M. Davidson, T. Poate, R. McCall, C. Blenkinsopp, and I. Turner, 2013: Observations of the swash zone on a gravel beach during a storm using a laser-scanner (Lidar). *J. Coastal Res.*, **65**, 636–641, https://doi.org/10.2112/SI65-108.1.

Anderson, D., A. S. Bak, K. L. Brodie, N. Cohn, R. A. Holman, and J. Stanley, 2021: Quantifying optically derived two-dimensional wave-averaged currents in the surf zone. *Remote Sens.*, **13**, 690, https://doi.org/10.3390/rs13040690.

Austin, M. J., G. Masselink, P. E. Russell, I. L. Turner, and C. E. Blenkinsopp, 2011: Alongshore fluid motions in the swash zone of a sandy and gravel beach. *Coastal Eng.*, **58**, 690–705, https://doi.org/10.1016/j.coastaleng.2011.03.004.

Bakhtyar, R., D. A. Barry, L. Li, D. S. Jeng, and A. Yeganeh-Bakhtiary, 2009: Modeling sediment transport in the swash zone: A review. *Ocean Eng.*, **36**, 767–783, https://doi.org/10.1016/j.oceaneng.2009.03.003.

Blenkinsopp, C. E., M. A. Mole, I. L. Turner, and W. L. Peirson, 2010: Measurements of the time-varying free-surface profile across the swash zone obtained using an industrial LIDAR. *Coastal Eng.*, **57**, 1059–1065, https://doi.org/10.1016/j.coastaleng.2010.07.001.

——, I. L. Turner, G. Masselink, and P. E. Russell, 2011: Swash zone sediment fluxes: Field observations. *Coastal Eng.*, **58**, 28–44, https://doi.org/10.1016/j.coastaleng.2010.08.002.

Bouguet, J.-Y., 2022: Camera calibration toolbox for MATLAB (1.0). CaltechDATA, https://doi.org/10.22002/D1.20164.

Brinkkemper, J. A., T. Lanckriet, F. Grasso, J. A. Puleo, and B. G. Ruessink, 2016: Observations of turbulence within the surf and swash zone of a field-scale sandy laboratory beach. *Coastal Eng.*, **113**, 62–72, https://doi.org/10.1016/j.coastaleng.2015.07.006.

Brocchini, M., and T. E. Baldock, 2008: Recent advances in modeling swash zone dynamics: Influence of surf-swash interaction on nearshore hydrodynamics and morphodynamics. *Rev. Geophys.*, **46**, RG3003, https://doi.org/10.1029/2006RG000215.

Brodie, K. L., B. Raubenheimer, S. Elgar, R. K. Slocum, and J. E. McNinch, 2015: Lidar and pressure measurements of inner-surfzone waves and setup. *J. Atmos. Oceanic Technol.*, **32**, 1945–1959, https://doi.org/10.1175/JTECH-D-14-00222.1.

Butt, T., and P. Russell, 1999: Suspended sediment transport mechanisms in high-energy swash. *Mar. Geol.*, **161**, 361–375, https://doi.org/10.1016/S0025-3227(99)00043-2.

——, and ——, 2000: Hydrodynamics and cross-shore sediment transport in the swash-zone of natural beaches: A review. *J. Coastal Res.*, 255–268.

——, ——, J. Miles, and I. Turner, 2007: Sediment transport processes in the swash zone of sandy beaches. *J. Coastal Res.*, **50**, 636–640, https://doi.org/10.2112/JCR-SI50-120.1.

Chardón-Maldonado, P., J. C. Pintado-Patiño, and J. A. Puleo, 2016: Advances in swash-zone research: Small-scale hydrodynamic and sediment transport processes. *Coastal Eng.*, **115**, 8–25, https://doi.org/10.1016/j.coastaleng.2015.10.008.

Chen, W., J. J. van der Werf, and S. J. M. H. Hulscher, 2023: A review of practical models of sand transport in the swash zone. *Earth-Sci. Rev.*, **238**, 104355, https://doi.org/10.1016/j.earscirev.2023.104355.

Chickadel, C. C., R. A. Holman, and M. H. Freilich, 2003: An optical technique for the measurement of longshore currents. *J. Geophys. Res.*, **108**, 3364, https://doi.org/10.1029/2003JC001774.

Cowen, E. A., I. Mei Sou, P. L.-F. Liu, and B. Raubenheimer, 2003: Particle image velocimetry measurements within a laboratory-generated swash zone. *J. Eng. Mech.*, **129**, 1119–1129, https://doi.org/10.1061/(ASCE)0733-9399(2003)129:10(1119).

Dooley, C., S. Elgar, B. Raubenheimer, and L. Gorrell, 2025: Estimating surfzone currents with near-field optical remote sensing. *J. Atmos. Oceanic Technol.*, **42**, 33–46, https://doi.org/10.1175/JTECH-D-24-0015.1.

Elfrink, B., and T. Baldock, 2002: Hydrodynamics and sediment transport in the swash zone: A review and perspectives. *Coastal Eng.*, **45**, 149–167, https://doi.org/10.1016/S0378-3839(02)00032-7.

Elgar, S., and R. T. Guza, 1985a: Observations of bispectra of shoaling surface gravity waves. *J. Fluid Mech.*, **161**, 425–448, https://doi.org/10.1017/S0022112085003007.

——, and ——, 1985b: Shoaling gravity waves: Comparisons between field observations, linear theory, and a nonlinear model. *J. Fluid Mech.*, **158**, 47–70, https://doi.org/10.1017/S0022112085002543.

——, B. Raubenheimer, and R. T. Guza, 2001: Current meter performance in the surf zone. *J. Atmos. Oceanic Technol.*, **18**, 1735–1746, https://doi.org/10.1175/1520-0426(2001)018<1735:CMPITS>2.0.CO;2.

——, ——, and ——, 2005: Quality control of acoustic Doppler velocimeter data in the surfzone. *Meas. Sci. Technol.*, **16**, 1889–1893, https://doi.org/10.1088/0957-0233/16/10/002.

——, C. Dooley, L. Gorrell, and B. Raubenheimer, 2023: Observations of two-dimensional turbulence in the surfzone. *Phys. Fluids*, **35**, 085142, https://doi.org/10.1063/5.0159170.

Guedes, R. M. C., K. R. Bryan, and G. Coco, 2013: Observations of wave energy fluxes and swash motions on a low-sloping, dissipative beach. *J. Geophys. Res. Oceans*, **118**, 3651–3669, https://doi.org/10.1002/jgrc.20267.

Harry, M., H. Zhang, C. Lemckert, G. Colleter, and C. Blenkinsopp, 2018: Observation of surf zone wave transformation using LiDAR. *Appl. Ocean Res.*, **78**, 88–98, https://doi.org/10.1016/j.apor.2018.05.015.

Henderson, C. S., J. W. Fiedler, M. A. Merrifield, R. T. Guza, and A. P. Young, 2022: Phase resolving runup and overtopping field validation of SWASH. *Coastal Eng.*, **175**, 104128, https://doi.org/10.1016/j.coastaleng.2022.104128.

Holland, K. T., J. A. Puleo, and T. N. Kooney, 2001: Quantification of swash flows using video-based particle image velocimetry. *Coastal Eng.*, **44**, 65–77, https://doi.org/10.1016/S0378-3839(01)00022-9.

Hughes, M. G., G. Masselink, and R. W. Brander, 1997: Flow velocity and sediment transport in the swash zone of a steep beach. *Mar. Geol.*, **138**, 91–103, https://doi.org/10.1016/S0025-3227(97)00014-5.

Ibaceta, R., R. Almar, P. A. Catalán, C. E. Blenkinsopp, L. P. Almeida, and R. Cienfuegos, 2018: Assessing the performance of a low-cost method for video-monitoring the water surface and bed level in the swash zone of natural beaches. *Remote Sens.*, **10**, 49, https://doi.org/10.3390/rs10010049.

Jackson, N. L., K. F. Nordstrom, and E. J. Farrell, 2017: Longshore sediment transport and foreshore change in the swash zone of an estuarine beach. *Mar. Geol.*, **386**, 88–97, https://doi.org/10.1016/j.margeo.2017.02.017.

Jessup, A. T., C. C. Chickadel, S. A. Talke, and A. R. Horner-Devine, 2013: Cohstrex: Coherent structures in rivers and estuaries experiment. *Coherent Flow Structures at Earth's Surface*, J. G. Venditti et al., John Wiley and Sons, 215–230.

Lanckriet, T., J. A. Puleo, G. Masselink, I. L. Turner, D. Conley, C. Blenkinsopp, and P. Russell, 2014: Comprehensive field study of swash-zone processes. II: Sheet flow sediment concentrations during quasi-steady backwash. *J. Waterway, Port, Coastal, Ocean Eng.*, **140**, 29–42, https://doi.org/10.1061/(ASCE)WW.1943-5460.0000209.

Martins, K., C. E. Blenkinsopp, H. E. Power, B. Bruder, J. A. Puleo, and E. W. J. Bergsma, 2017: High-resolution monitoring of wave transformation in the surf zone using a LiDAR scanner array. *Coastal Eng.*, **128**, 37–43, https://doi.org/10.1016/j.coastaleng.2017.07.007.

——, P. Bonneton, P. M. Bayle, C. E. Blenkinsopp, A. Mouragues, and H. Michallet, 2020: Surf zone wave measurements from lidar scanners: Analysis of non-hydrostatic processes. *J. Coastal Res.*, **95**, 1189–1194, https://doi.org/10.2112/SI95-231.1.

Masselink, G., and M. Hughes, 1998: Field investigation of sediment transport in the swash zone. *Cont. Shelf Res.*, **18**, 1179–1199, https://doi.org/10.1016/S0278-4343(98)00027-2.

——, and J. A. Puleo, 2006: Swash-zone morphodynamics. *Cont. Shelf Res.*, **26**, 661–680, https://doi.org/10.1016/j.csr.2006.01.015.

——, and P. Russell, 2006: Flow velocities, sediment transport and morphological change in the swash zone of two contrasting beaches. *Mar. Geol.*, **227**, 227–240, https://doi.org/10.1016/j.margeo.2005.11.005.

McCormack, T., J. Hopkins, B. Raubenheimer, S. Elgar, and K. L. Brodie, 2025: Remote sensing of wave-orbital velocities in the surfzone. *Coastal Eng.*, **195**, 104631, https://doi.org/10.1016/j.coastaleng.2024.104631.

McIlvenny, J., B. J. Williamson, I. A. Fairley, M. Lewis, S. Neill, I. Masters, and D. E. Reeve, 2023: Comparison of dense optical flow and PIV techniques for mapping surface current flow in tidal stream energy sites. *Int. J. Energy Environ. Eng.*, **14**, 273–285, https://doi.org/10.1007/s40095-022-00519-z.

O'Connor, C. S., and R. S. Mieras, 2022: Beach profile, water level, and wave runup measurements using a standalone Line-scanning, Low-Cost (LLC) LiDAR system. *Remote Sens.*, **14**, 4968, https://doi.org/10.3390/rs14194968.

O'Dea, A., and K. Brodie, 2024: Analysis of beach cusp formation and evolution using high-frequency 3D lidar scans. *J. Geophys. Res. Earth Surf.*, **129**, e2023JF007472, https://doi.org/10.1029/2023JF007472.

Perkovic, D., T. C. Lippmann, and S. J. Frasier, 2009: Longshore surface currents measured by Doppler radar and video PIV techniques. *IEEE Trans. Geosci. Remote Sens*, **47**, 2787–2800, https://doi.org/10.1109/TGRS.2009.2016556.

Power, H. E., R. A. Holman, and T. E. Baldock, 2011: Swash zone boundary conditions derived from optical remote sensing of swash zone flow patterns. *J. Geophys. Res.*, **116**, C06007, https://doi.org/10.1029/2010JC006724.

Puleo, J. A., R. A. Beach, R. A. Holman, and J. S. Allen, 2000: Swash zone sediment suspension and transport and the importance of bore-generated turbulence. *J. Geophys. Res.*, **105**, 17 021–17 044, https://doi.org/10.1029/2000JC900024.

——, G. Farquharson, S. J. Frasier, and K. T. Holland, 2003: Comparison of optical and radar measurements of surf and swash zone velocity fields. *J. Geophys. Res.*, **108**, 3100, https://doi.org/10.1029/2002JC001483.

——, T. E. McKenna, K. T. Holland, and J. Calantoni, 2012: Quantifying riverine surface currents from time sequences of thermal infrared imagery. *Water Resour. Res.*, **48**, W01527, https://doi.org/10.1029/2011WR010770.

——, and Coauthors, 2014: Comprehensive field study of swash-zone processes. I: Experimental design with examples of hydrodynamic and sediment transport measurements. *J. Waterway, Port, Coastal, Ocean Eng.*, **140**, 14–28, https://doi.org/10.1061/(ASCE)WW.1943-5460.0000210.

——, D. Cristaudo, A. Torres-Freyermuth, G. Masselink, and F. Shi, 2020: The role of alongshore flows on inner surf and swash zone hydrodynamics on a dissipative beach. *Cont. Shelf Res.*, **201**, 104134, https://doi.org/10.1016/j.csr.2020.104134.

Raffel, M., C. E. Willert, and J. Kompenhans, 1998: *Particle Image Velocimetry: A Practical Guide*. 1st ed. Springer, 255 pp.

——, ——, F. Scarano, C. J. Kähler, S. T. Wereley, and J. Kompenhans, 2007: *Particle Image Velocimetry: A Practical Guide.* 2nd ed. Springer, 448 pp.

Raubenheimer, B., 2002: Observations and predictions of fluid velocities in the surf and swash zones. *J. Geophys. Res.*, **107**, 3190, https://doi.org/10.1029/2001JC001264.

——, and R. T. Guza, 1996: Observations and predictions of run-up. *J. Geophys. Res.*, **101**, 25 575–25 587, https://doi.org/10.1029/96JC02432.

——, ——, S. Elgar, and N. Kobayashi, 1995: Swash on a gently sloping beach. *J. Geophys. Res.*, **100**, 8751–8760, https://doi.org/10.1029/95JC00232.

——, S. Elgar, and A. Muscalus, 2024: Time series of swashzone currents during DuneX, version v1. Zenodo, 16 December 2024, https://doi.org/10.5281/zenodo.14457084.

Rivillas-Ospina, G., A. Pedrozo-Acuna, R. Silva, A. Torres-Freyermuth, and C. Gutierrez, 2012: Estimation of the velocity field induced by plunging breakers in the surf and swash zones. *Exp. Fluids*, **52**, 53–68, https://doi.org/10.1007/s00348-011-1208-x.

Salatin, R., Q. Chen, B. Raubenheimer, S. Elgar, L. Gorrell, and X. Li, 2024: A new framework for quantifying alongshore variability of swash motion using fully convolutional networks. *Coastal Eng.*, **192**, 104542, https://doi.org/10.1016/j.coastaleng.2024.104542.

Senechal, N., G. Coco, K. R. Bryan, and R. A. Holman, 2011: Wave runup during extreme storm conditions. *J. Geophys. Res.*, **116**, C07032, https://doi.org/10.1029/2010JC006819.

Senin, P., 2008: Dynamic time warping algorithm review. Information and Computer Science Department University of Hawaii Tech. Rep. 855, 23 pp., https://csdl.ics.hawaii.edu/techreports/2008/08-04/08-04.pdf.

Sou, I. M., and H. Yeh, 2011: Laboratory study of the cross-shore flow structure in the surf and swash zones. *J. Geophys. Res.*, **116**, C03002, https://doi.org/10.1029/2010JC006700.

Stockdon, H. F., R. A. Holman, P. A. Howd, and A. H. Sallenger Jr., 2006: Empirical parameterization of setup, swash, and runup. *Coastal Eng.*, **53**, 573–588, https://doi.org/10.1016/j.coastaleng.2005.12.005.

Tauro, F., R. Piscopia, and S. Grimaldi, 2017: Streamflow observations from cameras: Large-scale particle image velocimetry or particle tracking velocimetry? *Water Resour. Res.*, **53**, 10 374–10 394, https://doi.org/10.1002/2017WR020848.

Thielicke, W., and E. J. Stamhuis, 2014: PIVlab—Towards user-friendly, affordable and accurate digital particle image velocimetry in MATLAB. *J. Open Res. Software*, **2**, 30, https://doi.org/10.5334/jors.bl.

Wang, K., and T. Gasser, 1997: Alignment of curves by dynamic time warping. *Ann. Stat.*, **25**, 1251–1276, https://doi.org/10.1214/aos/1069362747.

Willert, C. E., and M. Gharib, 1991: Digital particle image velocimetry. *Exp. Fluids*, **10**, 181–193, https://doi.org/10.1007/BF00190388.

Wilson, G. W., H. T. Özkan-Haller, R. A. Holman, M. C. Haller, D. A. Honegger, and C. C. Chickadel, 2014: Surf zone bathymetry and circulation predictions via data assimilation of remote sensing observations. *J. Geophys. Res. Oceans* , **119**, 1993–2016, https://doi.org/10.1002/2013JC009213.